Worth a Closer Look: Raman Spectra of Lead-Pipe Scale

Pasteris, Bae, Giammar, Dybing, Yoder, Zhao, and Hu

Supplemental Information

SI Table of Contents

Section 1. Supplementary figures and captions

Section 2. Sample information, file information, and spectral acquisition parameters keyed to all figures

Section 3. Brief introduction to Raman spectroscopy

Section 4. Instrumental details of the Raman microprobe system used in this study

Section 5. Accuracy and reproducibility in Raman spectroscopic analyses

Section 6. Precipitation experiments with Ca:Pb molar ratio of 20

Section 7. Luminescence encountered during Raman spectroscopic analysis

Section 1. Supplementary figures and captions

Fig. S1

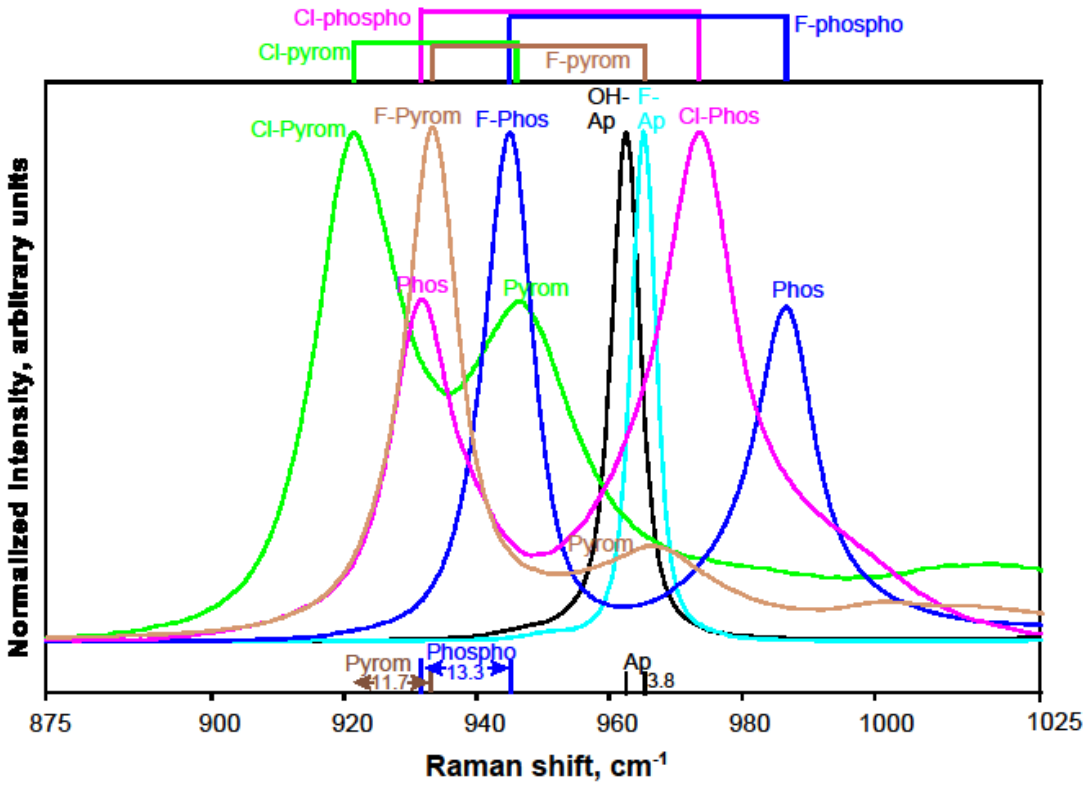


Figure S1: Three pairs of phosphate phases (OH- and F-apatite, Cl- and F-pyromorphite, and Cl- and F-phosphohedyphane) illustrate their spectral differences due to anion substitution. Along the bottom x-axis, the spectral offset between the 🖫$_1$ peak positions within each pair is shown, with offsets much greater for the Pb-bearing than the Ca-alone phosphates. Along the top x-axis, the spectral separation between the 🖫$_1$ and 🖫$_3$ peaks is shown for the pyromorphite and phosphohedyphane pairs, illustrating that both absolute peak position and 🖫$_1$-🖫$_3$ peak separation are very sensitive to anion substitution. (The 🖫$_3$ peaks for the Ca-apatites lie at higher wavenumbers than shown on this figure.)

Fig. S2

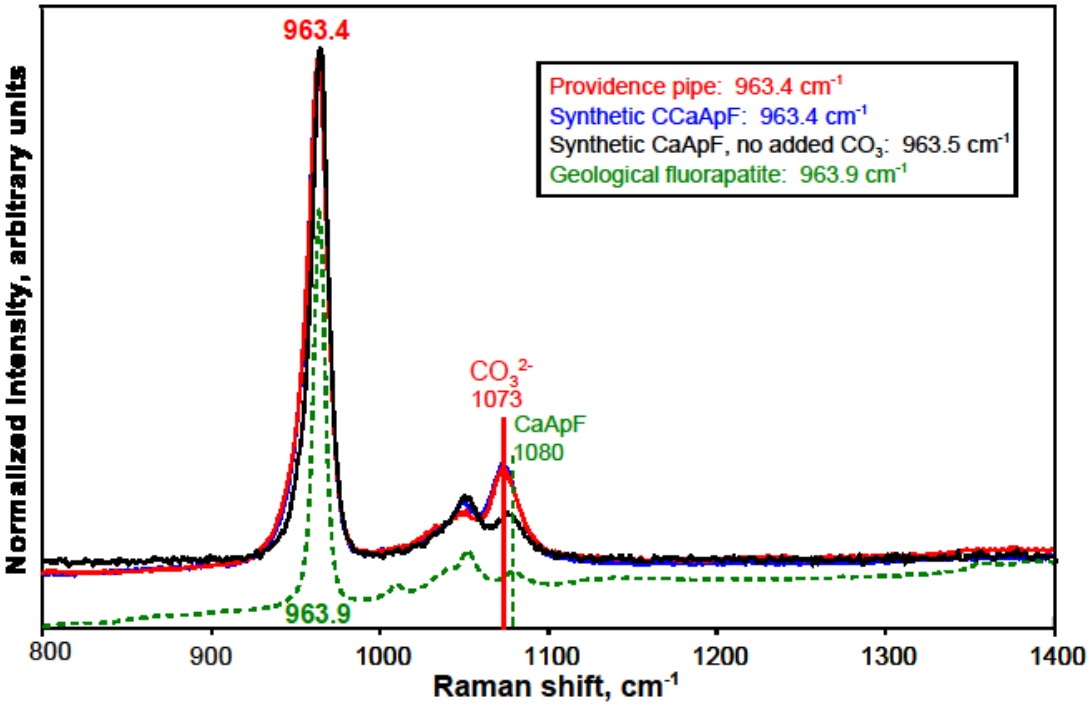
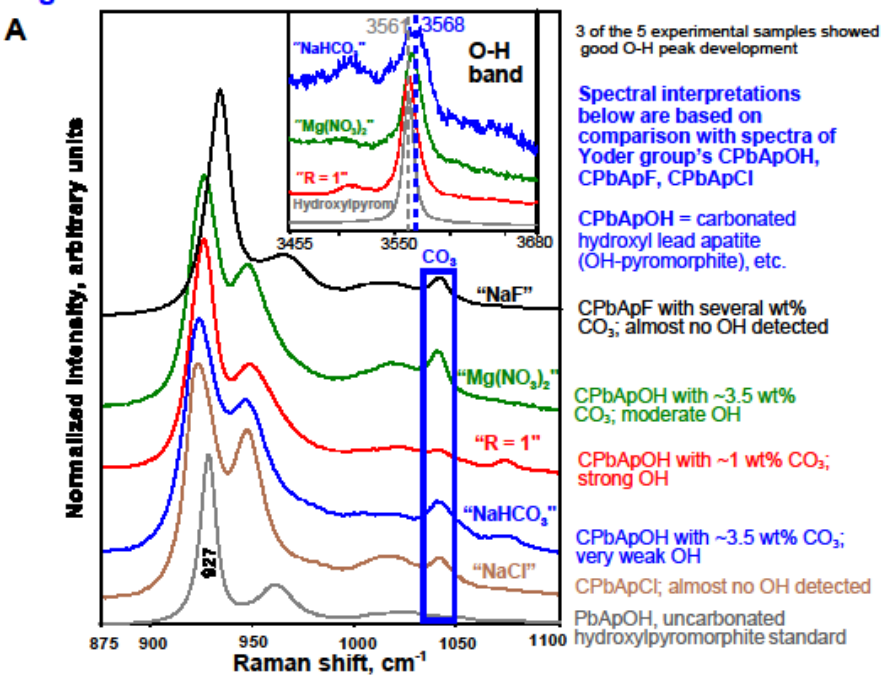


Figure S2: The red spectrum is of an in-situ analysis on surficial pipe scale in a harvested lead pipe from Providence, RI. The pipe had experienced 75 weeks of conditioning with synthetic water emulating that of the current Providence water system, with ongoing addition of orthophosphate beginning after week 45. This is the spectral signature of an apatite species, and the $\square_1$ peak position defines it as significantly F-bearing (Pasteris and Ding, 2009) [34]. The peak at about 1073 cm^{-1} indicates carbonate substitution for phosphate in the fluorapatite. Two spectra of synthetic fluorapatites have been superimposed on that of the Providence sample. The black spectrum is of a fluorapatite aqueously precipitated in the presence of air. The blue spectrum is of a fluorapatite precipitated from an aqueous solution with a 4:1 molar ratio of CO_3:PO_4. The close match between the blue spectrum and the pipe scale indicates that the fluorapatite scale has significant carbonate substitution. The narrower peak width of the synthetic sample without added carbonate (black) compared to the comparable carbonated sample (blue) demonstrates how the incorporation of carbonate induces disorder in the apatite structure. The dashed green spectrum at the bottom of the figure is of a geological fluorapatite from the Lake Baikal region in southeast Siberia. Two vertical lines indicate the spectral offset between the $\square_3$ band of fluorapatite at 1080 cm^{-1} (dashed green, aligned with geological uncarbonated fluorapatite's $\square_3$) and the carbonate band at 1073 cm^{-1} for the carbonated fluorapatite of the pipe scale (solid red line).

Fig. S3



B **All solutions prepared in air; supersaturated (Minteq calculation) with respect to $Pb_3(PO_4)_2$ and $PbHPO_4$. Additional supersaturated phases shown below (Zhao et al, 2018).**

Sample	Pb_T (M)	P_T (M)	NO_3^- (M)	Na^+ (M)	Mg^{2+} (M)	Cl^- (M)	F^- (M)	HCO_3^-	pH	Super-saturated phases
$Mg(NO_3)_2$	3.20 x 10^{-6}	3.20 x 10^{-4}	2.406 x 10^{-3}	5.516 x 10^{-4}	1.2 x 10^{-3}				7.0	$Pb(OH)_2$, hycer, OH-pyrom
NaF	3.20 x 10^{-6}	3.20 x 10^{-4}	6.4 x 10^{-6}	3.741 x 10^{-3}			3.2 x 10^{-3}		7.0	$Pb(OH)_2$, hycer, OH-pyrom
NaCl	3.40 x 10^{-6}	3.40 x 10^{-4}	6.8 x 10^{-6}	4.143 x 10^{-3}		3.6 x 10^{-3}			7.0	hycer, Cl-pyrom, OH-pyrom
$NaHCO_3$	6.44 x 10^{-6}	6.44 x 10^{-4}	1.29 x 10^{-5}	3.744 x 10^{-3}				3.1 x 10^{-3}	7.2	cerussite, hycer, OH-pyrom
R = 1 = Total P/Pb	2.46 x 10^{-5}	2.46 x 10^{-5}	3.85 x 10^{-3}	3.87 x 10^{-3}	hycer = hydrocerussite pyrom = pyromorphite				6.7	$Pb(OH)_2$, cerussite, hycer, OH-pyrom

Figure S3. Panel A is a stack of the spectra for the same synthetic pyromorphite samples shown overlapped in Figure 8. Additionally shown here are the OH-spectral window and more compositionally definitive spectroscopic interpretations of the individual samples aqueously precipitated from the solutions defined in panel B. Panel A is a re-drawing of the left portion of Figure 1B in Zhao et al (2018) [4]. Note in panel B that only a pyromorphite (OH, F, or Cl) species was detected by Raman (same for GIWAXS analysis), although all the sample solutions were calculated to be initially supersaturated with respect to additional phases (see table's heading and right-most column).

Fig. S4

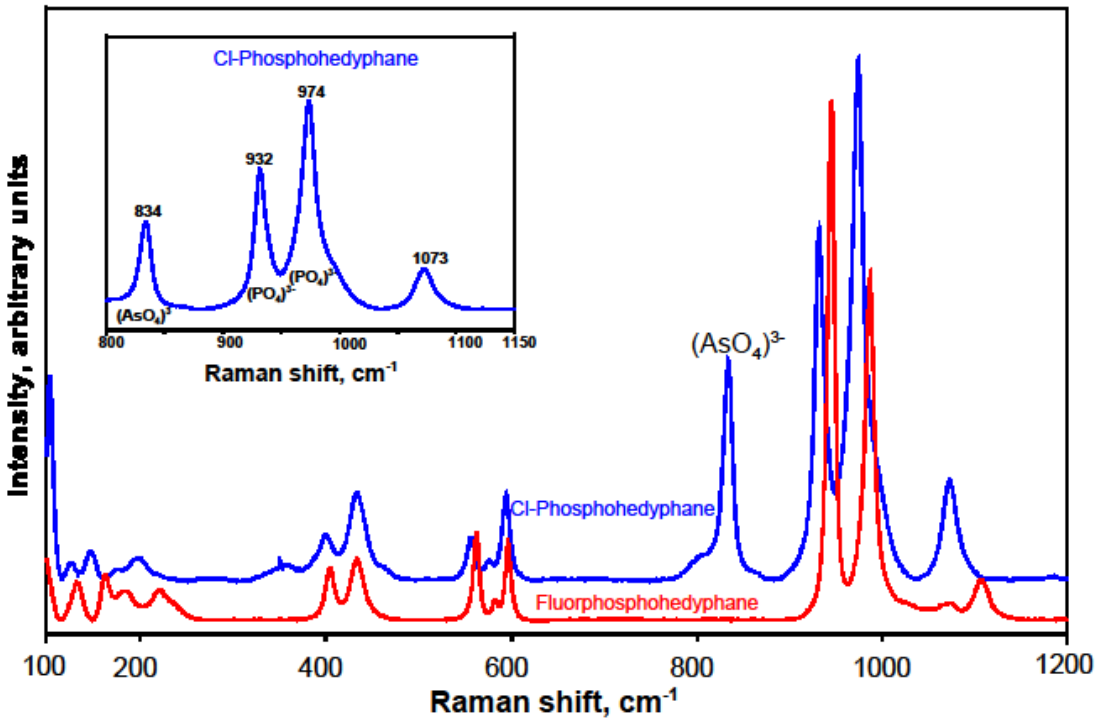


Figure S4: Stacked spectra of geological samples of chlorphosphohedyphane (upper spectrum in blue) and fluorphosphohedyphane (lower spectrum in red), both spectra background-corrected. The inset for the chlorphosphohedyphane clarifies the positions of the $(PO_4)^{3-}$ bands for the end-member form of that mineral and the $(AsO_4)^{3-}$ band for the arsenate substitution (probably for phosphate) in the natural mineral. Vanadate also substitutes readily in chlorphosphohedyphane, and it is a likely participant in lead-pipe scale in multiple localities (Gerke et al, 2009 [13]; Nadagouda et al, 2011 [10]; Orta, 2019 [62]; Tarr, 2019 [36]; Yoder et al, 2017 [60]).

Fig. S5

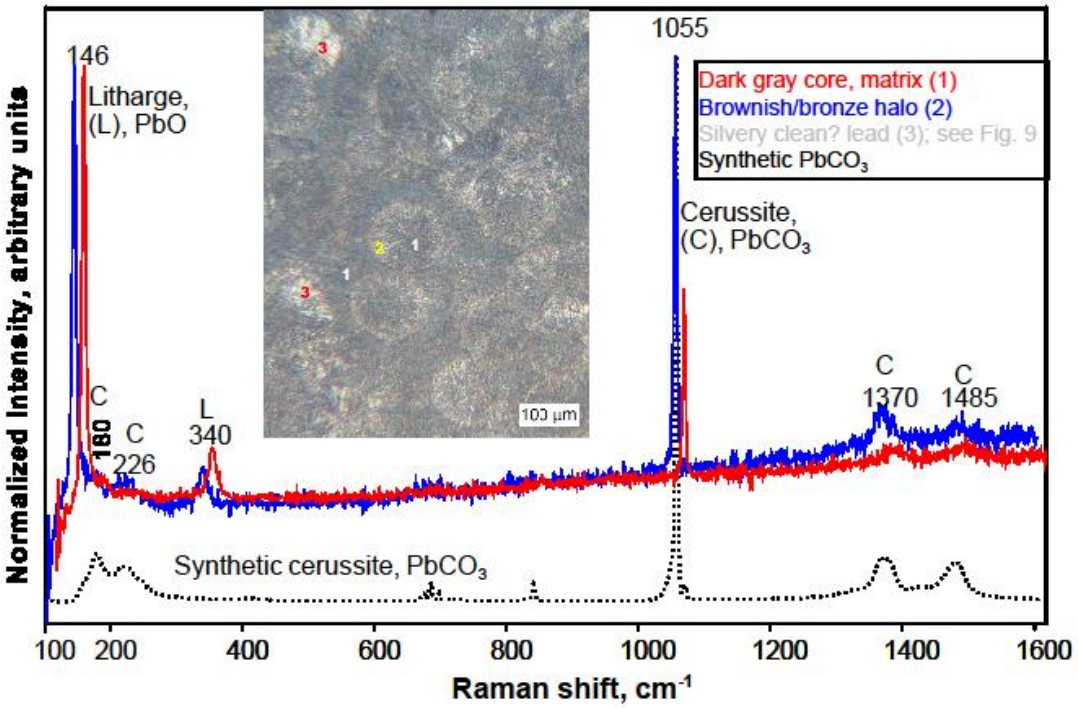


Figure S5: Experimental lead pipe harvested after treatment with synthetic D.C.-simulating water for 15 weeks. Reflected-light microscopy (see photo inset) shows patches of a dark-gray phase (labeled 1 in photo; red spectrum) encircled by a brownish rim (labeled 2 in photo; blue spectrum). Spectra of both optical features reveal litharge and cerussite, but in different ratios. Both spectra are normalized to the intensity of the litharge peak at 146 cm^{-1}. The red spectrum has been shifted slightly to the right of the blue one in order to reveal the differences in relative peak heights between the two dominant phases. The 226 cm^{-1} peak is a small, broad feature of cerussite, more abundant in the brown than in the dark gray material. For comparison, a spectrum of synthetic cerussite is at the bottom of the figure. For information on the highly reflective material labeled 3 in the photo, see Figure 10.

Fig. S6

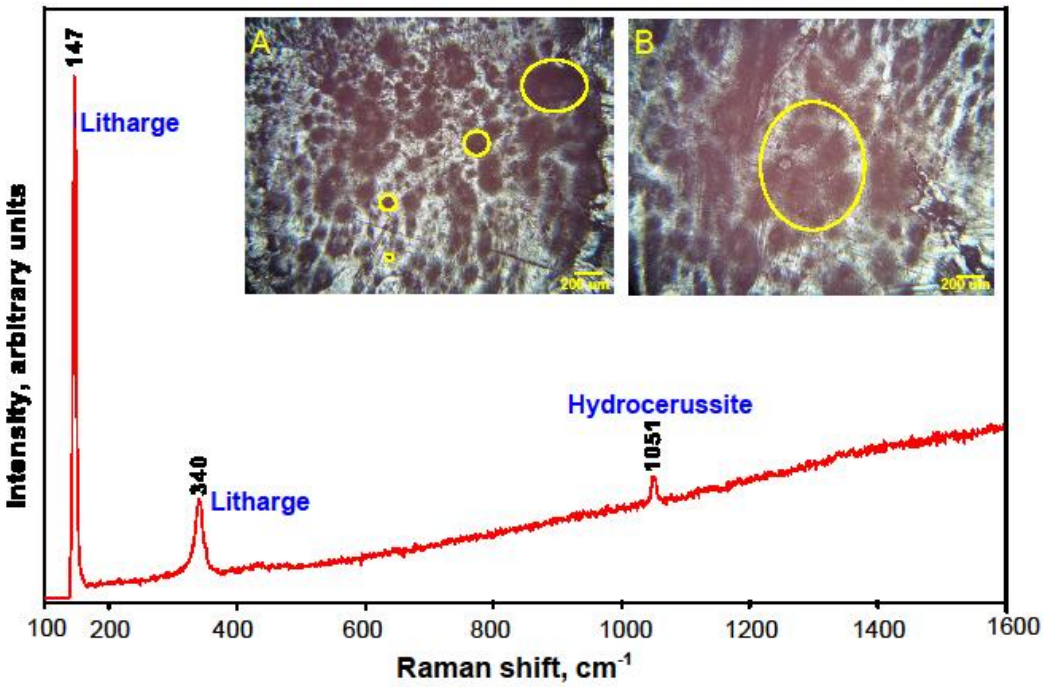


Figure S6: Photomicrographs taken in reflected light (A, B) of the weathered surface of a small, pure lead ingot that had sat exposed to air under laboratory room conditions for over 10 years. Note the similarity in mottled appearance between the surface of this sample and the experimental pipe surface shown in Figure S5's photo inset. As expected, the black regions are dominated by litharge, but also comprise a lead carbonate phase, in this case hydrocerussite. The latter is distinguished from cerussite by the position of its dominant C-O peak (at 1051 cm^{-1}) and its O-H peak (weak peak at 3544 cm^{-1}, not shown). Comparison of the photographs in Figures S5 and S6 suggests that the lead-scale minerals nucleate and grow at (random?) spatial intervals on the order of tens to hundreds of micrometers.

Fig. S7

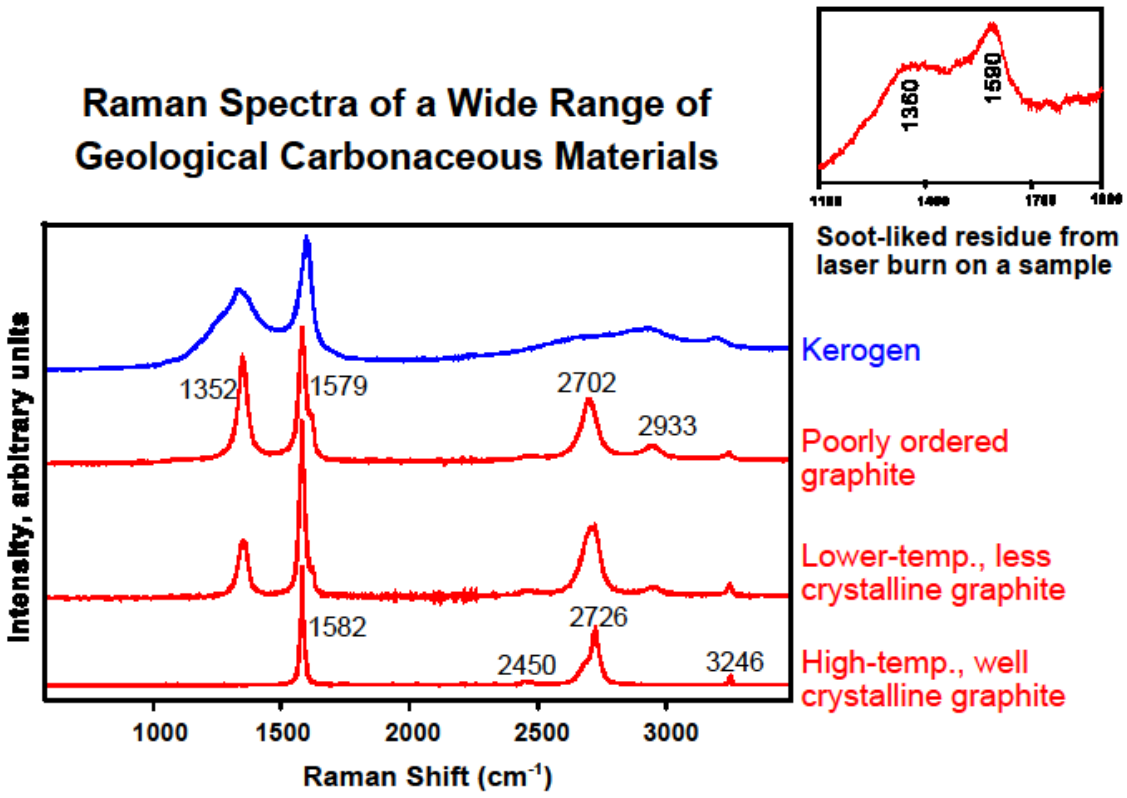


Figure S7: Raman spectra of geological carbonaceous materials illustrating differences in their degree of crystallinity. The most crystalline material (bottom spectrum) is high-quality graphite. The lowest degree of crystallinity is shown in the top spectrum, which is of a "raw" natural carbonaceous material called kerogen. Carbonaceous materials illustrate one example of the sensitivity of Raman spectra to the degree of atomic ordering (one aspect of crystallinity) among materials. In this case, the spectroscopic and physical differences among the samples reflect the temperature conditions under which they formed or were subsequently metamorphosed. For reference, the spectral inset in the upper right corner exemplifies the physically soot-like residue on one of our earlier synthetic samples due to laser irradiation that was too intense and/or too long in duration. The uppermost red spectrum with a peak labeled as 1579 cm^{-1} illustrates a small amount of laser-heating-induced downshifting compared to the bottom red spectrum with the comparable peak labeled as 1582 cm^{-1}.

Section 2. Sample information, file information, and spectral acquisition parameters keyed to all figures

Fig. 1: (A) The half-cylinder lead pipe segment was photographed by an iPhone7 (Apple Inc.) digital camera. (B) The microscale lead pipe cross-section is shown in a back-scattered electron image obtained by a JEOL scanning electron microscope operated at 15 kV (SEM, JEOL 7001LVF).

Fig. 2: Plattnerite, commercial (file 03118011), 1 mW laser power, 80x obj., 32x4s acquisitions. **Scrutinyite**, synthesized by Weiyi Pan and confirmed by XRD (file 03098006), 0.5 mW, 80x obj., 32x4s. **Minium**, commercial pigment (file 08218014_BL), 0.35 mW, 80x obj., 32x4s; baseline-corrected spectrum. **Massicot**, from heated litharge (file 03037024), 13.7 mW, 80x obj., 20x1s. **Litharge**, weathered lead ingot (file 06297022), 1 mW, 50x obj., 32x4s.

Fig. 3: a) **Litharge** on weathered lead ingot (file 06297022), 1 mW, 50x obj., 32x4s. b) **Litharge** in harvested pipe 22A (file 02247014), 5.4 mW, 50x obj., 20x1s. c) Clean lead ingot laser-heated to form **litharge+massicot** (file 06297026), >6 mW, 50x obj., 32x4s. d) Clean lead ingot laser-heated to form **massicot** (file 03037024), 13.7 mW, 80x obj., 20x1s.

Fig. 4: Spectra **a** and **b** taken in different areas on the wall of the same experimental lead pipe; 0.5 mW laser power, 80x obj., 32x4s. a) File 11157009. b) File 11157004. c) **Cerussite** standard, synthetic, confirmed by XRD (file 01308002), between 10 and 14 mW, 80x obj., 32x4s. d) **Hydrocerussite** standard, synthetic, confirmed by XRD (file 01308008), between 10 and 14 mW, 80x obj., 32x4s.

Fig. 5: **Hydroxylapatite** standard, Aldrich (file 06203004), 10.6 mW laser power, 80x obj., 32x4s. **Fluorapatite** standard from Lyle Gordon, confirmed by XRD, synthesized at high temperature in a CaF_2 flux with Ca_3PO_4 (file 07183005), 10.4 mW, 100x obj., 32x4s. **Hydroxylpyromorphite** with 1.4 wt% CO_3 substitution, synthetic, confirmed by XRD (file 03148005), 12.3 mW, 80x obj., 32x4s. **Chlorpyromorphite** with 2.75 wt% CO_3 substitution, synthetic, confirmed by XRD (file 01089019), 10.2 mW, 80x obj., 32x4s. **Fluorphosphohedyphane** from Anthony Kampf, geological, from Blue Bell Mine, San Bernadino, CA (file 10136013_BL), 14.9 mW, 80x obj., 32x4s; baseline-corrected spectrum. **Chlorphosphohedyphane** from Anthony Kampf, geological, from Capitana Mine, Chile, from holotype #55429 (file 10146002_BL), 14.8 mW, 80x obj., 32x4s; baseline-corrected spectrum.

Fig. 6: See spectral data above for Fig. 5.

Fig. 7: a) **Chlorphosphohedyphane** from Anthony Kampf, geological, from Capitana Mine, Chile, from holotype #55429 (file 10146002_BL), 14.8 mW, 80x obj., 32x4s; baseline-corrected spectrum. b) **Chlorapatite** standard from Lyle Gordon, confirmed by XRD, synthesized at high temperature in a $CaCl_2$ flux with Ca_3PO_4 (file 07183011), 10.4 mW, 80x obj., 32x4s. c) **"Unknown"** that is a Pb-bearing member of the apatite family, synthesized by Chao Pan, being compared here with Ca-apatite, pyromorphite, and phosphohedyphane standards (file 01207021), 13.5 mW, 50x obj., 32x4s; see SI section 6 for synthesis details. d) **Chlorpyromorphite** with 2.75 wt% CO_3 substitution, synthetic, confirmed by XRD (file 01089019), 10.2 mW, 80x obj., 32x4s.

Fig. 8: See spectral documentation for Fig. SI3.

Fig. 9: Synthetic carbonated pyromorphite standards, structure confirmed by XRD, carbonate concentration established by independent analytical laboratory. **a)** File 03148016_BL, 12.3 mW laser power, 80x obj., 32x4s. **b)** File 02018019_BL, 11.8 mW, 80x obj., 32x4s; baseline-corrected spectrum. **c)** File 01089019_BL, 10.2 mW, 80x obj., 32x4s; baseline-corrected spectrum. **d)** 01089036_BL, 10.2 mW, 80x obj., 32x4s; baseline-corrected spectrum.

Fig. 10: All spectra taken on the same conditioned pipe S1-E-Cylinder. 1 mW laser power, 50x obj., 20x1s. File numbers listed from the bottom spectrum upward are 05267027, 05267026, 05267025, 05267024, 05267018, and 05267023.

Fig. 11: a) Conditioned pipe 62w-26-3a, sample section of pipe wall 1 cm^2 (file 06018032), 0.5 mW, 80x obj., 32x4s**. b)** Conditioned pipe 62w-26-3a, sample section of pipe wall 1 cm^2 (file 06018029), 0.5 mW, 80x obj., 32x4s. **c)** Particle on filter (file 11107016), 0.55 mW, conditioned pipe 62w-26-3a, sample section of pipe wall 1 cm^2 (file 06018032), 0.5 mW, 80x obj., 32x4s.

Fig. S1: Samples, files, and acquisition parameters are all the same as in Figure 4, with the addition here of synthetic **fluoropyromorphite**, confirmed by XRD (file 02053027), 10.3 mW, 50x obj., 32x4s.

Fig. S2: Red (solid-line) spectrum, harvested pipe, not conditioned (file 06279006), 10 mW, 80x obj., 32x4. **Blue** (solid-line, almost coincident with red) spectrum, synthetic carbonated fluorapatite, confirmed by XRD (file 09240024), 7.2 mW, 50x obj., 32x4s. **Black** (solid-line) spectrum, synthetic fluorapatite, confirmed by XRD (file 07160019), 8.5 mW, 80x obj., 32x4 s. **Green** (dashed-line) spectrum, geological fluorapatite (file

11110407), between 10 and 15 mW, 80x obj., 32x4s.

Fig. S3: "NaF" (file 12307013), 13.2 mW laser power, 80x obj., 32x4s. **"$Mg(NO_3)_2$"** (file 10307004), 13.8 mW, 80x obj., 32x4s. **"R=1"** (file 11017008), 13.9 mW, 80x obj., 32x4s. **"$NaHCO_3$"** (file 11017013), 13.9 mW, 80x obj., 32x4s. **"NaCl"** (file 10307019), 13.8 mW, 80x obj., 32x4s. **Hydroxylpyromorphite** standard (file 03148005), 12.3 mW, 80x obj., 32x4s.

Fig. S4: Fluorphosphohedyphane from Anthony Kampf, geological, from Blue Bell Mine, San Bernadino, CA (file 10136013_BL), 14.9 mW, 80x obj., 32x4s; baseline-corrected spectrum. **Chlorphosphohedyphane** from Anthony Kampf, geological, from Capitana Mine, Chile, from holotype #55429 (file 10146002_BL), 14.8 mW, 80x obj., 32x4s; baseline-corrected spectrum.

Fig. S5: Region labeled 1 (red spectrum, shifted slight to right), file 05267012, 1 mW laser power, 50x obj., 20x1s. **Region labeled 2** (blue spectrum, matches up with the labels on x-axis), file 05267017, 1 mW laser power, 50x obj., 20x1s. **Cerussite** ($PbCO_3$) standard, synthetic, structure confirmed by XRD (file 01308002), 11.8 mW, 80x obj., 32x4s.

Fig. S6: Weathered surface of lead ingot (file 06297022), 1 mW laser power, 50x obj., 32x4s.

Fig. S7: Inset in upper right corner, laser burn (file 01317009), 13.5 mW laser power, 50x obj., 20x1s. Samples in **main panel** are all geological carbonaceous materials that were separated from rocks. Each sample powder was analyzed under conditions of

laser power and laser exposure time to minimize sample damage.

Fig. S8: See SI section 6 for the figure and its accompanying details.

Section 3. Brief introduction to Raman spectroscopy

Raman and infrared spectroscopies both characterize vibrational motions, such as stretching and bending, between covalently bonded atoms. They differ in the mechanism by which the frequency/energy of these vibrations is detected and by which symmetries of bonds can be detected by each spectroscopy. For Raman spectroscopy (RS), a monochromatic source of light, i.e., a beam of photons (typically from a laser), interacts with the sample and causes scattering. Most of the scattered photons (which can be directed to a sensitive detector via a microscope and accompanying optical system) retain the original wavelength/frequency/energy of the irradiating laser light. About 1 in 10^7 photons, however, scatters inelastically, losing an amount of energy that reflects the energy of vibration of the bonds within the sample. These losses of energy are recorded as shifts from the energy/wavelength of the laser's photons to that of the detected photons. The recorded photon output of such scattering interactions is plotted in a Raman spectrum showing intensity of scattered photons (y-axis) vs. the shift in photon energy (x-axis) in terms of wavenumber (in Δcm^{-1}), i.e., Raman shift. Such spectra act as reproducible, diagnostic fingerprints of solids, liquids, and gases that meet certain criteria (i.e., selection rules) for the nature of the bonds. For instance, totally ionic bonds cannot be detected by Raman spectroscopy, and the most strongly covalent bonds provide the strongest Raman signals. The energetics (and therefore

vibrational signatures) of these bonds are a function of the nature of the chemical interaction of the bonded atoms, the symmetry of both the bonds themselves and that of the overall structure of the phase/compound in which they reside, and the masses of the bonded atoms.

The Raman spectrum of a given compound is therefore a somewhat complicated result of multiple compositional and structural interactions that define its nature. A Raman spectrum is a combined chemical-structural fingerprint. The fingerprint aspect makes it useful in the identification of a compound, even to the point of distinguishing between polymorphs (as also accomplished by XRD). The sensitivity of the specific positions of the Raman bands to the chemical and structural environment of the bond under consideration, however, affords a much greater usefulness to the spectrum than just simple identification. For instance, the spectral bands will be offset (in predictable directions whose amounts can be calibrated against standards) due to compositional variations (solid solution) in different samples of the same mineral species, and the bands typically will broaden as the degree of atomic ordering or crystallinity decreases. Individual atoms/elements are not detected by Raman spectroscopy, but the effects of the substitution of a given element for the “typical” one in a compound can be seen as a change in the Raman spectrum. Such compositional substitutions not only change the frequency of vibration between a bonded pair of atoms (decreasing in wavenumber if the substituting atom has a greater mass than the typical one), but they also may change the chemical/energy environment for nearby bonded atoms; the latter case also leads to changes in spectral band position and width. The Raman spectrum is actually more sensitive to changes in chemical environment within a compound than it is

definitive for which specific element/atom(s) has changed.

There are many books that discuss Raman spectroscopy in much more detail and with focus on the theoretical background to the above phenomena. There are also multiple articles and chapters that illustrate the application of Raman spectroscopy to minerals, such as those discussed in this paper (Nasdala, et al., 2004 [26], 2012 [27]; Fritsch et al, 2012 [28]; Chou and Wang, 2017 [29]; Gazquez et al, 2017 [30]; Pasteris and Beyssac, 2020 [31]).

Section 4. Instrumental details of the Raman microprobe system used in this study

The Raman microprobe used for all the analyses in this study is a HoloLab Series 5000 Raman Microscope from Kaiser Optical Systems, Inc. (Ann Arbor, MI). The microscope is fiber-optically connected to the spectrometer system, which consists of a laser, gratings, and a detector. Excitation at 532 nm was delivered to the sample by a Coherent frequency-doubled Nd-YAG laser connected by an 8-μm-diameter, single-mode optical fiber to a research-grade Leica (Germany) microscope. The laser light was propagated downward to the sample. Raman-scattered (Raman-shifted) light was collected in a 180º back-scattered mode by the same optical objectives used to focus the laser on the sample, while 532-nm notch filters suppressed the further propagation of unshifted (Rayleigh-scattered) light. The Raman-scattered photons were collected by a 100-μm-diameter multimode optical fiber, which effectively acts as a pinhole. Upon entering the spectrometer, the Raman signal beam was split it into two component

beams. These passed through a volume holographic optical element that consists of two gratings, which dispersed each beam and imaged both of them simultaneously onto a thermoelectrically cooled CCD. The CCD array detector (1”x1”, Andor Technology, Ireland) has 2048 channels across its width; the 100-2500 cm^{-1} spectral region was imaged across the top of the CCD, and the 2500-4400 cm^{-1} region across the bottom. This configuration permitted simultaneous detection of the full 100-4400cm^{-1} spectrum at a spectral resolution of 2.5 cm^{-1} without moving gratings.

The accuracy of the program-corrected Raman wavenumber values was assured in several ways. The final (i.e., calibration-corrected) output of the absolute wavenumber values and the exact position of the laser wavelength were calibrated against the emission lines of Ar and Ne lamps. The relative wavenumber axis (i.e., cm^{-1} of Raman shift) was calibrated via reference to the known spectrum of cyclohexane, and the stability of the calibration was checked daily by monitoring of the peak position at 520.6 ± 0.1 cm^{-1} of a silicon wafer. The signal intensity scale across the entire spectrum was calibrated by reference to the known (externally calibrated) white-light spectrum of a tungsten lamp. The calibration corrections were applied immediately to each raw spectrum by the Kaiser Optical Holograms® software. The software also applied a dark-count correction curve for electronic noise; a new dark background file was acquired once every two hours. The typical time used for optimal S:N on fine-grained samples was 64 x 4 seconds (the input value of 32 x 4 seconds requires doubling in order to allow for software-controlled elimination of γ-ray impacts on the detector).

Section 5. Accuracy and reproducibility in Raman spectroscopic analyses

There are many different companies that currently market Raman instruments, and the optical configurations, lasers, detectors, other electronics, and software differ greatly among them. The details of the Raman laboratory-based instrument used in this study are provided in the section above, and they reflect several of the issues that control the accuracy (e.g., how "true" the detected peak positions are across the entire recorded spectrum; how true the ratios of peak areas are) and reproducibility (in count rate, peak shape, and peak position as recorded over time and under what conditions).

Peak position and reproducibility: Peak positions known to within a couple of wavenumbers are important for the fingerprint identification of a mineral/compound, gas species, liquid, or dissolved polyatomic species. Higher levels of accuracy and reproducibility, however, are required for the interpretation of measured peak positions as indicators of specific compositions of a compound, in which variations on the order of tenths of wavenumbers to several wavenumbers may be compositionally significant (as illustrated in multiple cases in this paper).

In addition to the calibration and software procedures mentioned in the SI section 4, it is important to have the following analytical procedures in place on a daily basis: 1) measure a standard sample, traditionally the main peak of a polished silicon wafer (which does not tarnish and whose opacity and surface polish assure easy signal optimization upon careful focusing), and record the wavenumber of its peak position (i.e., midpoint at half-maximum intensity) to one or two decimal places; 2) maintain close control on the temperature (ideally ±0.5 ºC) of the instrument/laboratory so that

expansion and contraction of the optical elements do not cause shifts in the recorded wavenumbers; 3) follow the same acquisition protocol as much as possible in all analyses, while assuring high S:N ratio as well as the stability of the sample under the laser (controlled by its power and duration).

In this paper, peak positions are typically shown to the nearest 0.1 cm^{-1} because the specific positions have compositional meaning, and our Raman instrument maintains a peak reproducibility on a silicon wafer of ±0.15 cm^{-1} as measured over a period of weeks or more. This degree of reproducibility is possible in large part because the laboratory temperature can be maintained so well and our Raman instrument has no moving parts, i.e., no gratings that need to be rotated back and forth into the desired spectral position.

Assessing percent of polyatomic substitution: Values for the wt% CO_3 substitution in several types of metal phosphate compounds are given in this paper. These evaluations are based on comparisons with appropriate standard samples whose CO_3 concentrations have been externally determined by an independent commercial laboratory (Galbraith Laboratories, Inc., Knoxville, TN). The procedure for evaluating the amount of such substitution is based on the ratio of the areas of two peaks (actually specific spectral bands deconvolved from the peaks) within the sample, in this case the main C-O stretching band of CO_3 and the main P-O stretching band of PO_4.

Section 6. Precipitation experiments with Ca:Pb molar ratio of 20

The precipitate from an aqueous solution containing 30 mM phosphate, 30 mM calcium, 1.5 mM lead, and 2.1 mM chloride was prepared by Chao Pan as part of a series of precipitates from Ca-Pb-PO_4-Cl solutions of various compositions. The precipitate was formed upon dropwise addition of a phosphate solution into a solution that contained dissolved calcium, lead, and chloride over the course of ten minutes. During the addition process the solutions were sparged with N_2 to prevent introduction of CO_2, and the pH was periodically adjusted to a target pH of 5.5 by addition of dilute solutions of NaOH or HNO_3. Reagents used to prepare the solutions were Na_2HPO_4, NaH_2PO_4, $Ca(NO_3)_2$, $Pb(NO_3)_2$, and NaCl. The resulting suspension was centrifuged, and the solids were washed three times by resuspending the solids in deionized water, centrifuging the suspension, and decanting the supernatant. The remaining solids after washing were freeze-dried before being analyzed by X-ray diffraction (see Figure S8 below) and Raman spectroscopy (see Figure 7). A portion of the solids was digested in concentrated nitric acid for quantitative determination of the calcium and lead compositions by inductively coupled plasma mass spectrometry (PerkinElmer DRC II).

The resulting solid had a Ca/Pb atomic ratio of 0.51, which is in contrast to the Ca/Pb ratio of 20 for the solution from which the solids precipitated. This indicates a nearly 40-fold enrichment of the precipitated solid in lead relative to the initial solution. The X-ray diffraction pattern of the solid had the general pattern of peaks for pyromorphite, but the specific positions of the peaks were not those for pure pyromorphite (see Figure S8). The patterns also were not good matches for any pure

apatite solids or phosphohedyphane. These results and interpretations can be compared to those for Figure 7 in the text.

Fig. S8

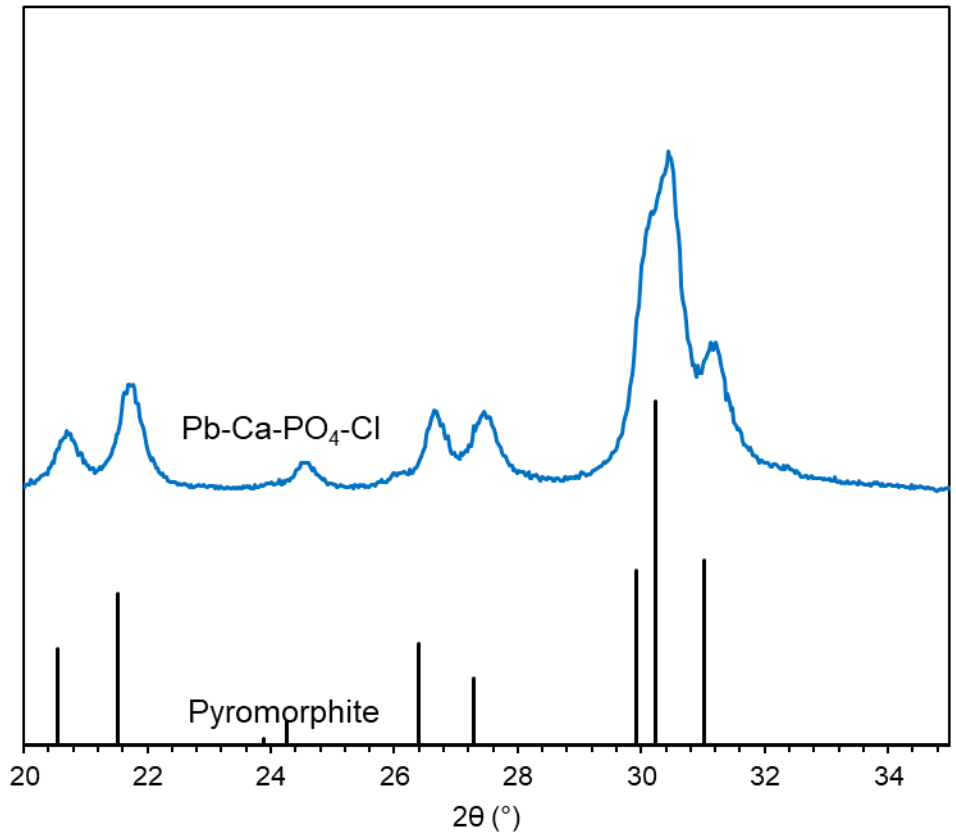


Figure S8. X-ray diffraction pattern of a solid with a Ca:Pb ratio of 0.51 that was precipitated from an aqueous solution with a Ca:Pb ratio of 20 (30 mM Ca and 1.5 mM Pb) and 2.1 mM chloride upon addition of 30 mM phosphate. For reference the pattern for pyromorphite is shown.

Section 7. Luminescence encountered during Raman spectroscopic analysis

It is important to realize that the detector on a Raman instrument is not limited to detecting only Raman scattered photons but rather records all photons within its wavelength range of detection sensitivity. Thus, not all the peaks and broad humps that appear in an acquired spectrum need be Raman spectroscopic signals. Stray light from the computer screen, for instance, may be seen as spurious narrow peaks.

The most prominent non-Raman features typically recorded arise from laser-induced luminescence. This can be caused by the inherent mineral/compound properties of specific grains in the sample or by their accompanying "contaminants" such as organic compounds. The electronic structure of minerals and the quantized nature of electron levels allow for excitation (via an external energy source, such as a laser) of an electron to a higher-energy state. Such elevation is followed by the electron's return to its ground state with the accompanying release of the amount of energy that had enabled its rise. That released energy is luminescence of a certain wavelength. Such electron transitions are more readily enabled in some elements than others, e.g., rare-earth elements (REE) and other transition elements. There are multiple specific mechanisms by which luminescence, sometimes referred to as fluorescence in the Raman literature, can occur. For instance, certain elements/ions can be activators (e.g., Mn^{2+}); defect structures, such as produced by displacement of ions from their charge-balancing positions, create traps for electrons that consequently exhibit new allowed energy states (Rakovan and Waychunas 1996 [37]).

For the Raman analyst, such luminescence effects typically produce two different

kinds of interference with the desired Raman spectrum. Some luminescence peaks are just as narrow as Raman peaks, and therefore can cause confusion in identification of a given grain. In other cases, the luminescence creates a very broad spectral region of elevated background (a huge hump up to 100s of wavenumbers across) or a background count rate that steadily increases with increasing wavenumber. Such elevation in background causes a decrease in S:N, because noise increases as a function of the square root of background intensity. Fluorescence/luminescence can be up to 10^7 times stronger than a Raman signal. It therefore may be impossible to acquire a useful Raman spectrum in some circumstances; the relatively low-intensity Raman peaks can be "swallowed up" by the noise associated with the luminescence-elevated background. Very strong luminescence also can be created by some organic compounds and materials, especially those exhibiting conjugated carbon double bonds.

There are some work-arounds for the above situations. 1) Use of a laser of different wavelength may mitigate the problem. a) The new excitation wavelength may induce less luminescence in the specific sample, making it easier to detect the Raman bands. b) The actual wavelength at which Raman scattering occurs is a function of the excitation wavelength. So as to capture the inherent vibrational information of interest, as well as to present Raman spectra that are identical regardless of the excitation wavelength, Raman bands are always displayed along the x-axis in terms of their displacement from the excitation wavelength. In contrast, luminescence bands tend not to shift as a function of excitation wavelength (as long as the photon energy is sufficient to induce luminescence). This means that the mutual spatial/spectral relation between the Raman and the luminescence bands along the x-axis will change if the laser

wavelength is changed. The luminescence bands will appear to jump to a new part of the spectrum (only because the x-axis is labeled in wavenumber-shifts, not absolute wavenumbers), whereas the Raman bands will appear to remain in (shift) place. Such a laser switch therefore will reveal which bands are due to luminescence. This observation can eliminate confusion about which ones are the Raman bands, and the overlap of Raman and luminescence bands may be eliminated. A broad-featured luminescent feature, in turn, may “move away” from the Raman bands or be reduced in intensity upon a change in laser wavelength. 2) “Photo-bleaching” frequently decreases the intensity of broad-featured luminescence. If there is not a concern for laser-damage to the sample, the laser should be left focused on the desired grain, while the background count rate is monitored and (hopefully) decreases. The new S:N can be evaluated in a Raman spectrum taken after 5 or more minutes of irradiation. It is necessary to check for laser damage before and after taking that new spectrum, but the x-y-z position of laser focus must not be changed or the luminescence will suddenly increase again.